Correlation between the surface infrared radiation and deformation characteristics of oil shale during uniaxial compression

Shaoqiang Yang, Dong Yang*, Jing Zhao

Key Lab of In-situ Property-improving Mining of Ministry of Education, Taiyuan University of Technology, Taiyuan 030024, China

Abstract. The emission of infrared radiation from oil shale is, compared with other rocks, more intense due to the anisotropy during deformation. In this research, cracks in oil shale specimens were scanned with computed tomography (CT) scanning equipment, and the infrared radiation from their surface, as well as surface strain during uniaxial compression were analyzed. The results show that the specimens surface temperature constantly changes. Prior to the fluctuation of the internal stress of a test specimen, the temperature curve exhibits varying degrees of decline. Then the curve abruptly rises close to the specimen's point of failure. By analyzing the coefficient of variation of the surface temperature distribution of the specimens, it was found that the turning point on the curve from the horizontal fluctuation to rapid increase can serve as a warning of impending specimen failure. In a low-stress state, the location of a crack is indicative of the low-temperature infrared anomaly. With increasing stress, the high-temperature infrared anomaly will appear at the crack tip. Near the failure of the specimen, the appearance of an anomalous infrared precursor on its surface is related to the mode of failure. A high-temperature infrared precursor will occur in a shear failure zone, while a low-temperature infrared precursor will occur in a tensile zone. These regularities are very important to be taken into account to understand the development of the internal fracture network and deformation of oil shale deposits during in-situ pyrolysis.

Keywords: in-situ pyrolysis, infrared radiation, oil shale anisotropy, digital speckle, uniaxial compression.

1. Introduction

Oil shale is a fine-grained rock containing organic matter (also known as kerogen), which mainly consists of algae deposited under anaerobic conditions [1]. Being considered an unconventional energy source, shale oil has become more and more important as a substitute for traditional crude oil, in view of

---

* Corresponding author: e-mail *yangdong@tyut.edu.cn*

the decreasing production of conventional oil and gas and increasing demand for clean energy [2–4]. Under high-temperature conditions (around 450 °C), kerogen will be pyrolyzed into shale oil and mixed hydrocarbon gas [5]. The in-situ superheated steam mining technology that utilizes this process has been proposed by Zhao and co-researchers at the Taiyuan University of Technology and has been described in the paper by Kang et al. [6]. The method consists in heating oil shale by injecting superheated steam into the deposit through an injection borehole and transporting thereafter the pyrolyzed shale oil to the production borehole. As oil shale is a sedimentary rock which has been formed through the compaction of silt and clay particles and its matrix permeability is very low [7, 8], fractures in it are the main channels for the migration of superheated steam and oil and gas products. Therefore, the creation of a rich fracture network in oil shale deposits by hydraulic fracturing has become important to ensure efficient oil and gas production.

Hydraulic fracturing involves various mechanical processes such as fracture initiation and propagation, and is accompanied by changes in rock mechanical properties and pore pressure [9]. Oil shale tends to exhibit mechanical anisotropy due to the orientation of mineral particles, layering, the existence of microcracks and low aspect ratio pores and the presence of kerogen [10, 11]. This anisotropy has a direct effect on wellbore stability, perforation direction, hydraulic fracture expansion [12, 13], and even on the migration of superheated steam in a later period. Therefore, it is of great importance to study the mechanical properties of oil shale to enable determination of the most appropriate areas for its hydraulic fracturing and in-situ pyrolysis.

The determination of the uniaxial compressive strength of oil shale plays a key role in the study of wellbore stability and fracture propagation laws [14, 15]. It is well known that oil shale contains a large number of bedding planes, pores and fissure structures. It is to be expected that the mechanical response during the deformation process will be related to the orientation of the bedding and the distribution of internal fissures. Using computed tomography (CT) scanning technology, Zhou et al. [16] analyzed the fracture structure of oil shale specimens during uniaxial compression perpendicular and parallel to the bedding. The results showed that the cracks were mainly tensile when the loading was along the bedding, whereas shear cracking took place during the loading perpendicular to the bedding. Yan et al. [17] used ultrasonic technology to measure the axial and lateral velocities of oil shale specimens with different coring angles during uniaxial compression. The researchers found that the strength of oil shale first decreased and then increased with the widening of the coring angle, while Young's modulus and Poisson's ratio increased continuously. Shi et al. [18] used the Split-Hopkinson pressure bar (SHPB) system to test the dynamic tensile strength of black shale specimens when loaded at different angles to the stratification. The results showed that the failure mode was related to the loading direction. When θ was between 0° and 30°, the matrix suffered tensile failure, and when θ was between 30° and

90°, the specimens became prone to tensile-shear failure. These results were indicative of that the internal stratification of oil shale and the primary pores and fracture structures in it evoked the rock's mechanical anisotropy during the deformation process.

The accumulation, transformation, dissipation and release of energy during deformation are in part expressed in the form of acoustic emission, electromagnetic radiation, radiofrequency (RF) radiation and optical radiation [19]. By analyzing these energies, it is possible to determine the physical structure and stress state of the rock, thereby gaining knowledge of its deformation and fracturing characteristics [20]. Infrared thermal imaging technology (IRT) enables the surface temperature of an object to be recorded by capturing the radiation waves from its surface, giving this method the advantages of being non-destructive, real-time and non-contact [21]. A variety of studies have clarified the relationship between thermal emission and rock deformation. Wang et al. [22] determined the stress intensity corresponding to the predicted point of failure of limestone during cumulative uniaxial compression, and found it to be 89.5% of the peak stress intensity. By using IRT, Zhao and Jiang [23] studied changes in the acoustic emission and infrared radiation from bump-prone coal during its uniaxial compression and cyclic loading. The results showed that the stress values corresponding to infrared precursors were 90% and 82% of the peak stress during uniaxial and cyclic loading, respectively. Wu et al. [24], who also employed IRT, investigated the relationship between the average temperature and deformation of marble and granite under uniaxial compression. The researchers found that the thermal infrared (TIR) anomaly was positively correlated with press when the deformation (failure) was compressive or shear, while this correlation was negative when the deformation (failure) was tensile. The above studies have demonstrated that, indeed, the intensity of infrared radiation from a rock sample undergoes changes during deformation and failure. In addition, it was established that this change was related to the type and failure mode of the rock. But to date, there are no studies on changes in the intensity of infrared radiation from oil shale, in which natural bedding, pores and fissure structures appear during deformation.

This paper aims to study the effect of internal primary bedding planes, pores and fissure structures on the deformation of and infrared radiation from oil shale surface during the loading perpendicular and parallel to the bedding. First, CT scanning equipment was used to scan oil shale specimens in these two planes to determine the distribution of internal fracture structures in them. Subsequently, the specimens were subjected to uniaxial compression perpendicular and parallel to the bedding, and infrared radiation and deformation were recorded by an infrared thermal (IRT) imager and a digital speckle system, respectively. In this study, infrared thermal imaging equipment is employed to provide a theoretical basis for understanding the development of the internal fracture network and deformation of oil shale deposits during in-situ pyrolysis.

2. Experimental equipment and methods

2.1. Experimental equipment

The CT scanning system used in this experiment is a CT225k VFCB with a magnification of 1–400 times and a rotation angle resolution of 655360 steps/rev (Fig. 1a). The loading system is a WDW-E microcomputer-controlled electronic universal testing machine. The maximum test force is 200 kN. The accuracy of the test force indication is ±0.5%.The infrared thermal imaging system is a portable IRT imager manufactured by Intratec Company, Germany. Long-wave uncooled radiation detectors have a spectral range of 7.5–14 μm and their thermal sensitivity may reach 0.03 deg. The ARAMIS optical three-dimensional deformation measurement system (GOM Company, Germany) is used for strain measurement. The image acquisition rate may reach 500 Hz, the resolution of the charge-coupled device (CCD) camera is 1280 × 1024, the strain measurement range is 0.01–100% and its precision is 0.01%. The CT scanning equipment and its arrangement can be seen in Figure 1b.
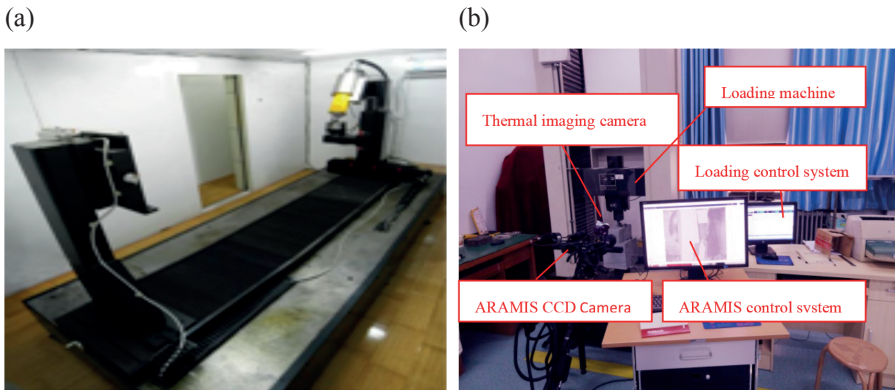
(a)   (b)

Fig. 1. Layout of CT scanning equipment: (a) micro-CT experimental system, (b) infrared thermal imager, speckle system and loading system.

2.2. Experimental method

The samples for the study were collected from the Fushun West oil shale open-pit mine, Fushun City, Liaoning Province, China. Before the experiment, oil shale was machined into 25 × 25 × 50 mm cuboid specimens with a sand wire cutting machine, and the end surface irregularity was less than 0.05 mm, as shown in Figure 2a. Six specimens with directions perpendicular and parallel to the bedding were selected and numbered V_1–V_6 and P_1–P_6, respectively. The relationship between the loading direction and the bedding is shown in Figure 2b and Figure 2c. Before the experiment, the front surface of the specimen was sprayed with white and gray paints to make the artificial speckle surface, as shown in Figure 2a. To reduce the influence of heat conduction and
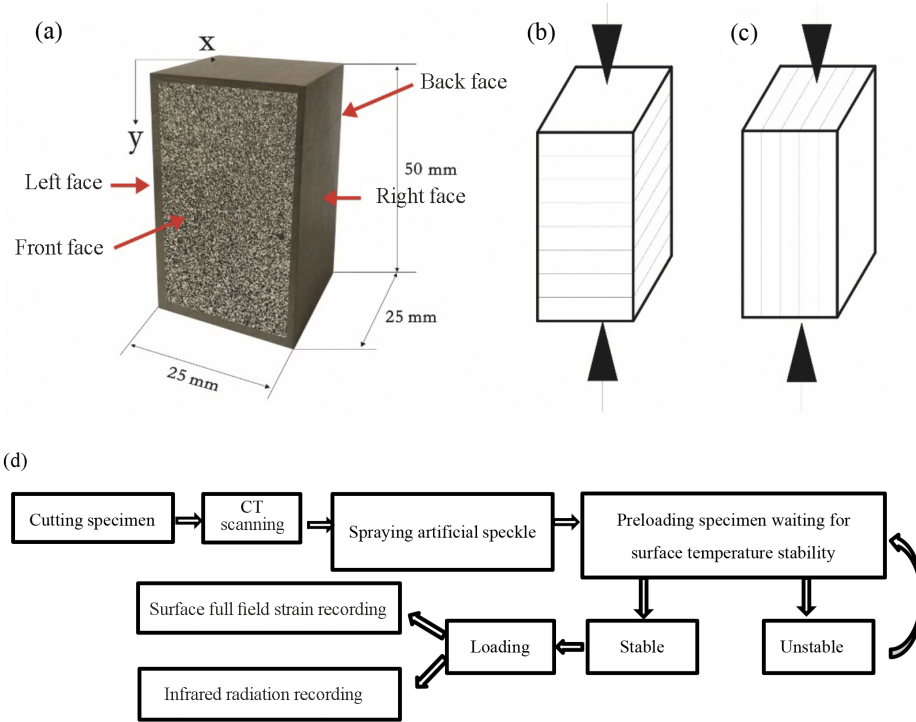
Fig. 2. Specimen and flow chart: (a) photo of oil shale after making an artificial speckle; (b)–(c) schematic diagrams of the relationship between loading direction and bedding; (d) flow chart of the experiment.

air convection between the end of the press machine and the specimen, the specimen was padded with an asbestos plate at both ends and then placed in the box which was filled with insulating materials to reduce the impact of ambient temperature changes on test results. The temperature and strain were measured through the pre-opened holes in the box. During the experiment, the press was loaded at a constant rate of 0.08 mm/min, and the surface strain and temperature data were collected by the speckle apparatus and infrared thermal imaging equipment. The experimental process is shown in Figure 2d.

2.3. Theoretical interpretation

The deformation of rock caused by external forces includes elastic deformation and inelastic deformation.

Based on the thermoelastic effect, under adiabatic conditions, the sum of temperature and principal stress satisfies a linear relationship [19], as shown in Equation (1):

$$\Delta T = -\frac{\alpha}{\rho c_\sigma} TS, \tag{1}$$

where ΔT is the change in temperature, K; T is the surface absolute temperature of the loaded solid, K; α is the factor of linear expansion, K^{-1}; ρ is the mass density, kg m^{-3}; C_σ is the specific heat coefficient under constant stress, J kg^{-1} K^{-1}, and S is the sum of principal stresses. The specimen is subjected to the axial pressure σ_1 only, and the lateral pressure σ_2 is zero. Therefore, the change in principal stress is related only to σ_1.

The dissipation of internal energy during rock deformation is a comprehensive effect of thermoelasticity and plasticity. The external work is not entirely converted into internal heat energy in the material, and most of this work is consumed in the process of internal microstructure change. In the process of plastic deformation, energy consumption mainly includes the following three parts, as shown in Equation (2) [25]:

$$\Delta E = \Delta E_1 + \Delta E_2 + \Delta E_3, \tag{2}$$

where ΔE is the total energy of internal consumption. ΔE_1 is the energy carried by the process of pore gas escape. Almost all rocks have specific pore and fracture structures in which CH_4, CO_2, CO, O_2 and other gases are mixed. With the deformation of pores and fractures caused by external forces, gas removes part of the heat during the process of escape from the internal free or adsorbed state, which leads to a decrease in temperature. Therefore, in general, $\Delta E_1 < 0$. ΔE_2 is the energy consumed in the processes of collapse of primary pores, propagation of cracks and initiation of new fractures in rocks, so, $\Delta E_2 < 0$. ΔE_3 is the energy generated by friction heating. In the process of plastic deformation, the relative displacement between the free surfaces, such as pores, cracks, joints and mineral particles, results in frictional heat generation under the action of external forces, and part of the energy is released in the form of thermal energy; therefore, $\Delta E_3 > 0$.

3. Results and discussion

The specimen sizes and peak stresses are given in Table. Since the peak strengths of V_5, P_4 and P_6 differ greatly from those of other specimens, in calculating the average peak stress these are ignored. As oil shale contains abundant pores and fracture structures, which gives evidence of obvious mechanical anisotropy, the average peak stress intensity in the perpendicular bedding direction is 1.3 times that in the parallel bedding direction.

Table. Specimen size and peak stress

Type of bedding	Specimen number	Specimen size, mm	Peak stress, MPa	Average peak stress, MPa
Perpendicular bedding	V_1	24.79 × 25.0 × 49.0	55.25305	54.1164
	V_2	24.92 × 24.80 × 49.62	53.95221	
	V_3	24.66 × 24.50 × 49.24	57.36989	
	V_4	24.92 × 24.96 × 49.32	51.21287	
	V_5	24.32 × 24.60 × 49.32	30.9689	
	V_6	24.82 × 24.84 × 49.22	52.7941	
Parallel bedding	P_1	24.78 × 24.94 × 49.94	40.21468	42.7014
	P_2	25.36 × 25.0 × 49.22	41.49369	
	P_3	24.58 × 25.0 × 48.94	46.08918	
	P_4	24.9 × 24.96 × 49.0	28.862	
	P_5	25.0 × 25.0 × 49.82	43.00832	
	P_6	24.42 × 24.98 × 49.82	24.5897	

3.1. Surface temperature variation with stress loading perpendicular to the bedding direction

The surface temperature of the specimen is stored in the infrared image in matrix form. We use self-programming to extract information from the temperature image and analyze it by using three statistical parameters: average temperature, maximum temperature and the coefficient of variation (CV). CV is used to measure the dispersion of surface temperature. The calculation method is described by Equation (3):

$$CV = \frac{\sigma}{\mu},\qquad(3)$$

where σ represents the standard deviation of surface temperature and μ represents the average temperature of the specimen. Because of the large number of specimens, only the test results for representative samples V_1 and P_2 are discussed.

Based on the variation in surface temperature and the coefficient of variation with stress illustrated in Figures 3 and 4, the entire loading process for specimen V_1 is divided into three stages. Because the average temperature curve is similar to the maximum temperature curve, the temperature curve in this paper includes the maximum temperature and the average temperature for the convenience of illustration.
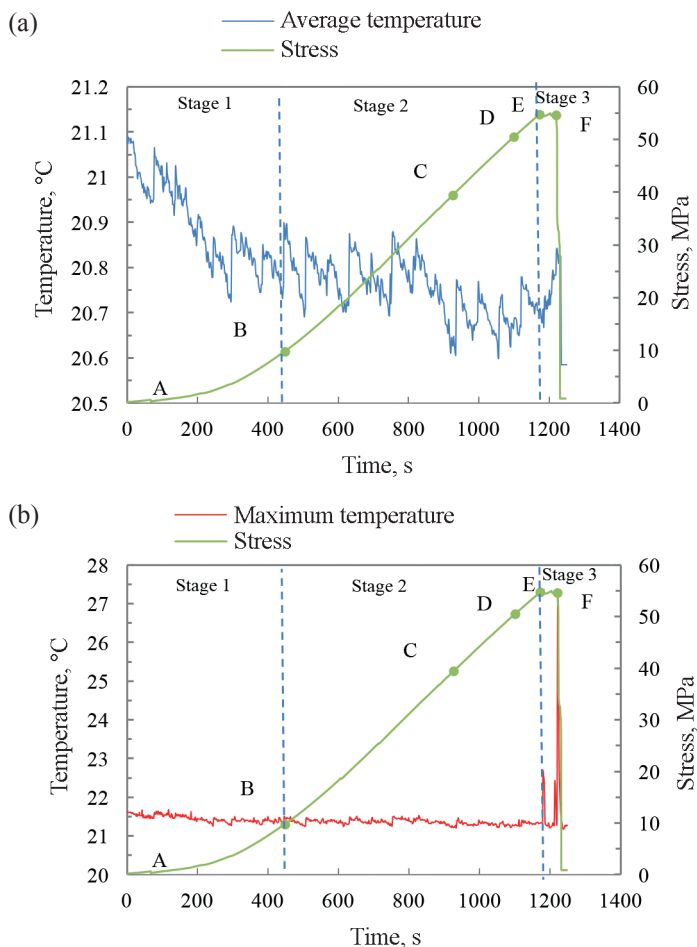
(a)

(b)

Fig. 3. Curves of surface temperature and stress versus time for specimen V_1.

Stage 1 is the compression stage. The stress curve assumes a concave shape, accounting for one-third of the entire loading process, and the stress reaches 17.2% of the peak stress. In this time period, the temperature curves abruptly decline, and the rate of decline decreases after 294 s. Meanwhile, the CV curve steeply rises; during the 200–300 s period, it jumps up frequently and then the rate of rise decreases. This occurs because almost all rocks, especially sedimentary minerals, contain pore and fissure structures of different scales, in which gases like CH_4, CO_2, CO and O_2 are present in certain amounts in free or adsorbed state [26]. In this low-stress stage, the process of gas escape from open fractures consumes part of the heat during fracture closure, resulting in a steep decline of the temperature curve [25, 27]. The nonuniform distribution of cracks leads to the temperature decrease of different degrees at each point of the specimen surface and increases the surface temperature dispersion,

which is the reason for the steep rise of the CV curve. When a fracture closes to a certain extent, mineral particles that fill in the fracture squeeze and slide between the fracture surfaces until they reach a stable or broken state [28]. This process is accompanied by frictional heating and energy release, which reduces the degree of cooling near the crack to a certain extent, resulting in the decrease in the rate of the temperature curve decline and CV curve ascent.

Stage 2 represents a linear elastic strain stage. As seen from Figure 3, in the period B–C, the temperature curve first fluctuates horizontally. After the loading has proceeded for 800 s, the curve slopes steeply downward, and then declines smoothly past C. When loaded to D, the average temperature curves rebound slightly and then continue to slope down smoothly. It is to be noted that the maximum temperature curve begins to fluctuate at this time. From Figure 4 it can be seen that the CV curve starts to fluctuate in this stage, however, the fluctuation is quite insignificant. This occurs because in the elastic stage, the temperature decreases due to the energy consumption by pore deformation and the temperature increases due to the thermal elasticity reaching a dynamic equilibrium, so, the temperature curve fluctuates horizontally [22]. When the stress reaches a certain value, the internal pores of oil shale collapse, which creates new channels for gas to escape from the pores. Meanwhile, the gas adsorbed in the pore begins to desorb [25]. At this point, the temperature decrease caused by the consumption of energy by the deformation and collapse of pores and desorption and escape of gas is much greater than the temperature increase caused by the increase in thermal elasticity, so the temperature curve slopes steeply downward [22, 28]. As the gas emission decreases, the energy loss also decreases; thus the temperature curve declines smoothly. The rise of the maximum temperature curve after time D may be due to the frictional heat effect and local energy release along the pore and fracture positions in the specimen in a high-stress state, resulting in the increase in maximum temperature [19, 22, 29]. Pore structures of different scales are scattered inside the oil shale specimen, and in the elastic stage, the temperature decrease caused by the collapse of pores and desorption and escape of gas has little effect on the positions of pores and fractures in it, so, the CV curve slopes up very smoothly.

Stage 3 is the yield stage. As Figure 4 shows, in this stage, the temperature and CV curves start to slope upward steeply, especially when the maximum temperature curve starts to jump frequently. At the moment of rupture, the maximum temperature reaches 27.18 °C. This occurs because simultaneously with the specimen failure, its internal pores and cracks constantly expand and penetrate, which leads to the continuous disruption of the internal stress balance [22, 29]. At this time, there occurs mainly the frictional deformation of specimens which slides along the shear plane, the fracture surface and mineral particles squeeze and rub against each other, which means that the frictional heat generation and energy release are mainly focused on the fracture surface, thus causing the temperature and CV curves to steeply rise in this stage [16, 19, 30].
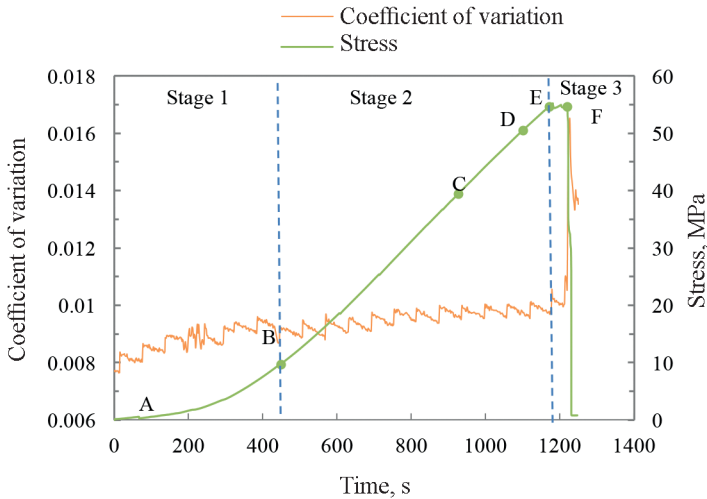
Fig. 4. Relationship between stress and surface temperature coefficient of variation for specimen V_1.

3.2. Surface temperature variation with stress loading parallel to the bedding direction

Figure 5a and Figure 5b show that the temperature curves of specimen P_2 decline approximately linearly from the beginning of the experiment to time J. It is to be noted that in the time period H–I, the maximum temperature curve slopes steeply up and the temperature increases 0.4 °C. Meanwhile, the CV curve turns upward following its horizontal fluctuation at time H (Fig. 6). According to Equation (2), there is a linear relationship between the change in temperature and the sum of the principal stresses in the elastic stage [19, 28]. Under the condition of equal displacement loading, in the low-stress stage, it can be assumed that the heat generated by thermal elasticity and the heat carried away by the escaping gas are both constant per unit time and have the same effect on the surface temperature of the specimen; thus, the temperature curves decline linearly, and the CV curves undergo almost no change. From time H, the internal cracks in the specimen begin to expand along the weak bedding planes, occurring mainly in the form of tensile splitting [16]. At this moment, there appears deformation inconsistency between different beddings which is accompanied by energy release. The change of rock surface temperature is related to its failure mode, tension failure can lead to a decrease in temperature and compression can lead to an increase in temperature [31]. The heterogeneity of oil shale causes different temperature changes at different locations, which leads to the abnormally steep rise of the temperature curve [23]. The CV curve also starts to slope upward.
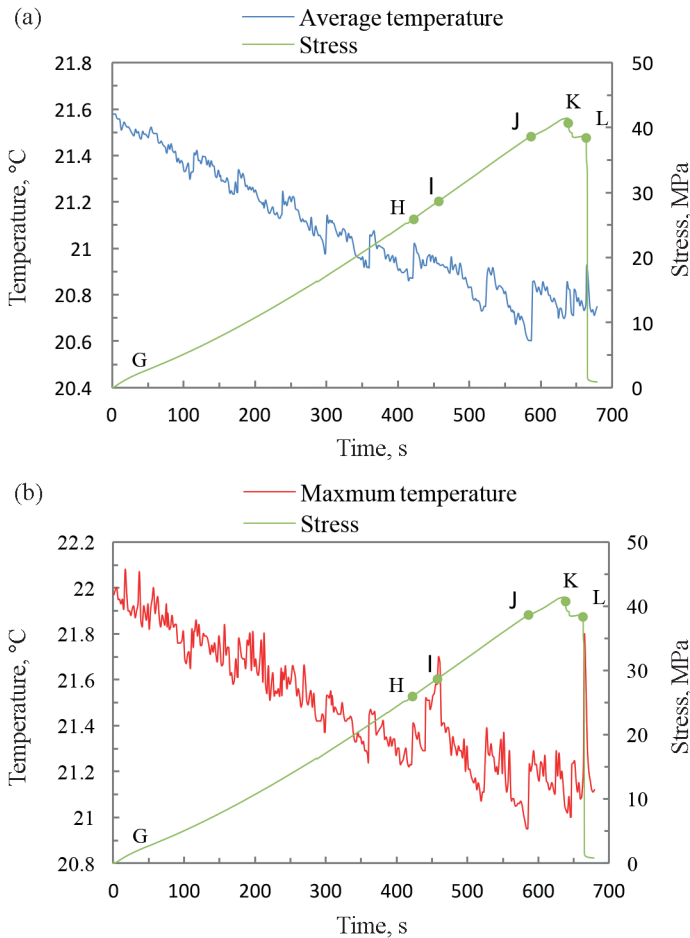
Fig. 5. Curves of surface temperature and stress versus time for specimen P_2.

After time J the stress curve fluctuates and slopes down to 0 at time L, the rates of the decline of the average and maximum temperature curves decrease and the maximum temperature curve starts to jump frequently. Before the destruction of the specimen at approximately 10 s, the curves start to rise steeply. At the moment of failure, the average and maximum temperatures increase respectively 0.2 °C and 0.89 °C. At this time, the rate of ascent of the CV curve in Figure 6 is also significant. The reason behind this is that during the stress fluctuation, the microcracks in the specimen begin to expand and merge into larger cracks, and the friction between the crack surface and the broken mineral particles generates heat [17]. This also explains why the temperature curve declines and the maximum temperature curve jumps constantly. However, because the temperature increases mainly around the cracks and on the shear plane [28], the surface temperature dispersion increases and the CV curve thus rises sharply.
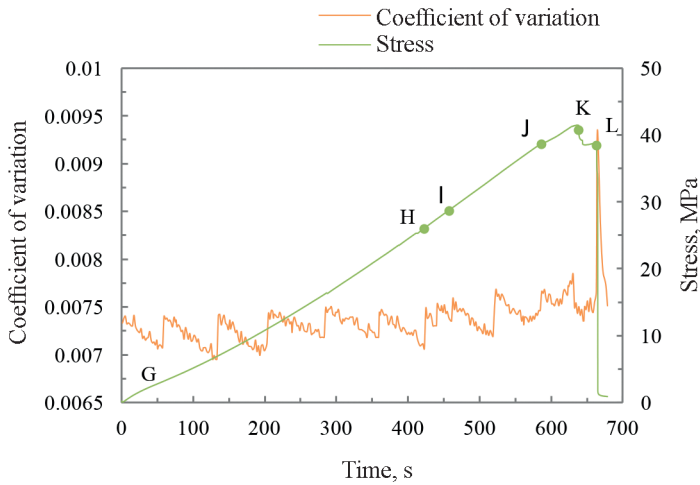
Fig. 6. Relationship between stress and surface temperature coefficient of variation for specimen P_2.

3.3. Temporal and spatial evolution characteristics of surface temperature and strain

The deformation and failure of rock are the result of its internal damage and crack propagation, accompanied by the accumulation and release of energy. As a transversely isotropic rock, oil shale contains a large number of pores and fractures, which inevitably leads to differences in surface strain and infrared radiation temperature. To study the relationship between these two parameters, the surface infrared thermal image and full-field strain diagrams of specimens V_1 and P_2 under different stress states (corresponding to the time marked on the stress curves in Figs. 4–6) are taken for analysis (Figs. 7–8).

As shown in Figure 7, a low-temperature zone appears in the lower part of specimen V_1 during the A–B period, and the average surface temperature decreases by approximately 0.25 °C. According to the strain diagram, the horizontal strain on the specimen surface is low, and the vertical strain near the crack is high. This occurs because when the stress is low, the cracks developed along the bedding inside the specimen close under the action of external force, resulting in the inconsistent deformation of the specimen surface [32]. At the same time, the gas inside the cracks is forced to escape and consume part of the energy, which leads to the appearance of a low-temperature zone in the infrared image of the specimen surface.

During the C–E period, the surface temperature of the specimen decreases further. At times C and D, a vertical low-temperature zone appears on the surface of the specimen. At time E, the low-temperature zone on the right is more clearly seen, and a high-temperature zone appears at the corresponding

position of the tip of the original crack in the 40th CT image of specimen V_1 (Fig. 9a). According to the specimen's strain diagram (Fig. 7) and picture after failure (Fig. 9c), the above phenomena are caused by tensile cracks at locations of higher horizontal strain. When oil shale undergoes tensile failure, this failure process consumes the energy accumulated during the compression of the specimen, which will lead to the emergence of vertical low-temperature zones [25, 31]. However, at the crack tip, the heat generated by friction increases the temperature.

Infrared anomalies appear again in the central part of the specimen before failure. At this time, the strain is relatively high at position 2 as labeled in the vertical strain diagram (Fig. 7), which corresponds to the pore position in the 240th layer in the CT image in Figure 9b. At the same time, a high-strain
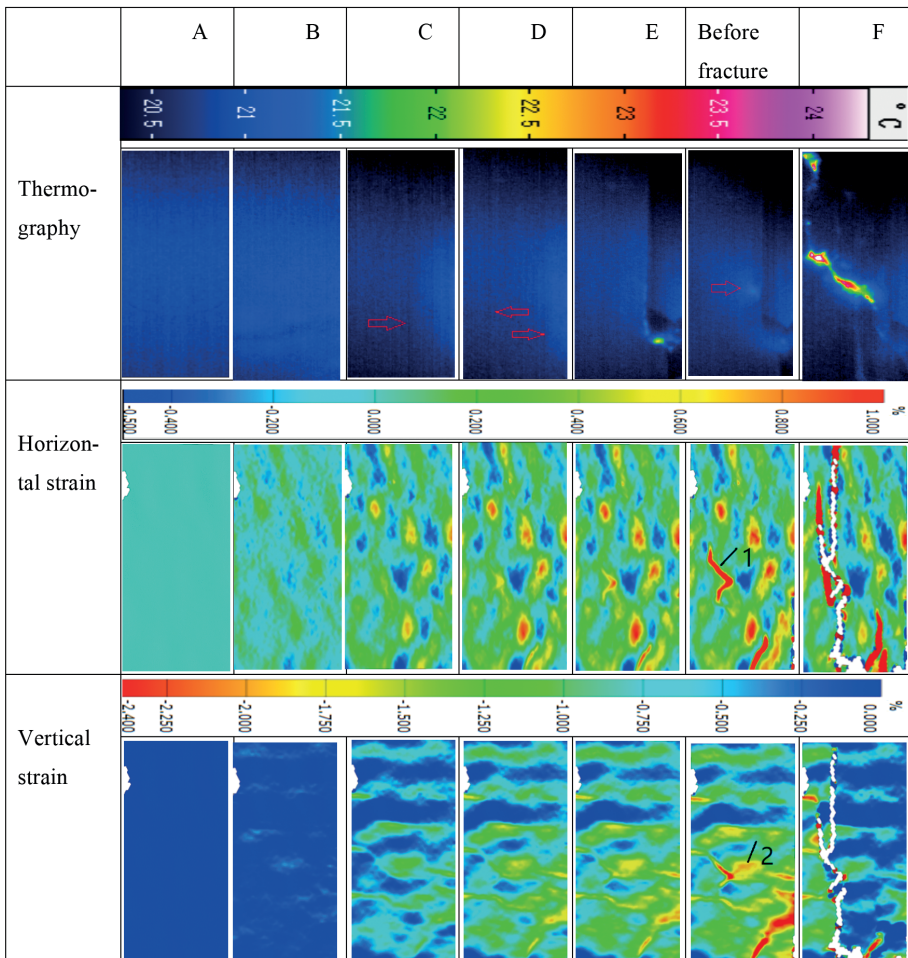

Fig. 7. Infrared radiation and strain diagram of the surface of specimen V_1.

region appears at position 1 as labeled in the horizontal strain diagram (Fig. 7). Then, at time F, the temperature on the shear surface along position 1 increases sharply from position 2 in the infrared image. This occurs because with increasing stress inside the specimen, the primary pores are destroyed first, which is accompanied by the release of energy and the frictional heating of mineral particles in the process of destruction [19, 22]; thus, the infrared anomaly appears in this area. Since the tensile strength of rock is much lower than its compressive strength, the rock is destroyed along the high horizontal strain, generating frictional heat on the failure surface, thus causing the temperature to increase [31].

Figure 8 shows that the infrared radiation temperature on the surface of specimen P_2 decreases as the stress increases. During the period from H to I, the temperature in the specimen's middle part is obviously higher than that in
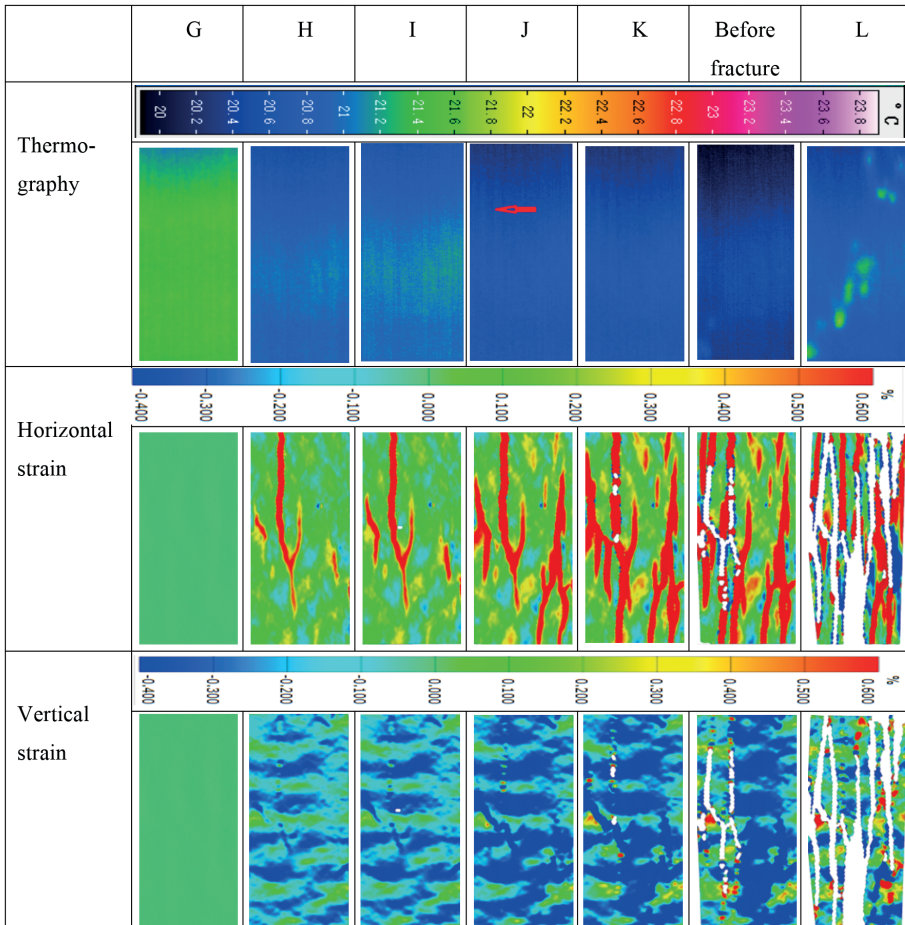

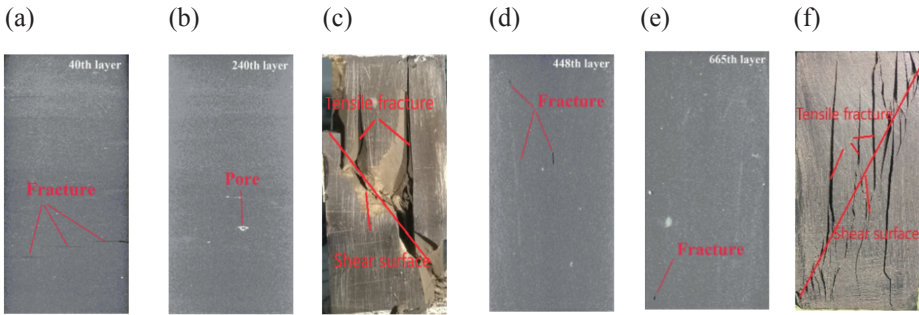Fig. 8. Infrared radiation and strain diagrams of the surface of specimen P_2.

(a)   (b)   (c)   (d)   (e)   (f)

Fig. 9. CT scanning diagrams and failure photos of specimens: (a)–(c) V_1; (d)–(f) P_2.

other parts, indicating infrared anomaly. At this point, the vertical strain on the left side of the specimen is slightly higher than that on its right side, and a high-strain region appears on the left side of the horizontal strain diagram, which corresponds to the position of the primary crack shown in Figure 9d. This occurs due to the fact that when the loading takes place in the direction of bedding, the axial cracks can propagate freely along the axial direction, while in the low-stress state, the initial cracks will produce tensile splitting along the bedding plane [16, 17]. So, the deformation at the plane of weakness and the crack position is more obvious than that at the other positions on the specimen surface under parallel lamination loading, resulting in its inconsistency. When the stress increases to a certain value, the microcracks inside the specimen begin to expand. The readjustment of internal stress is accompanied by the generation of frictional heat and the release of energy, which results in infrared anomaly [22].

With increasing vertical strain, a low-temperature zone appears at time J at the point indicated by an arrow in the infrared image in Figure 8. At this time, two high horizontal strain zones develop vertically on the specimen surface. Compared with the photo of the specimen shown in Figure 9f, as the stress increases, the temperature of the crack location decreases because of the high amount of energy consumed in the high horizontal strain region [23, 25, 28]. After time K, infrared anomaly appears in the lower-left corner and the middle part of the specimen in its infrared thermal image. The position of infrared anomaly corresponds to the original crack in the 656th layer of the CT image in Figure 9e. Due to the local failure of the specimen, the internal energy is released to a certain extent, which makes its surface temperature drop again. At time L, the surface temperature increases, and there appears a high-temperature zone along the diagonal line. The strain diagram analysis reveals that the above phenomena are caused by that the high horizontal strain region expands in the vertical direction and passes through the upper and lower parts of the specimen as the stress increases. When the stress peak is reached, the temperature decreases due to the high amount of energy

consumed in the process of crack propagation along the bedding plane, while the increase of temperature on the shear plane is mainly affected by frictional heating. Therefore, the temperature in the tensile failure zone decreases and the shear surface temperature rises. However, the temperature of the specimen surface decreases before failure, which may be caused by the relaxation of stress produced by the readjustment of internal stress after local failure [22].

4. Conclusions

Under uniaxial compression, the surface temperature of rocks with relatively high integrity such as sandstone and granite increases with increasing stress. Conversely, the surface temperature of sedimentary rocks with natural fractures like oil shale exhibit phased characteristics and anisotropy with increasing stress.

Based on the results of study, the following conclusions can be drawn:

1. Change in surface temperature during oil shale deformation is caused by the combined action of pore deformation, fracture propagation, frictional heat generation and gas escape from pores. When an oil shale specimen is loaded perpendicular to the bedding, its surface temperature decreases rapidly during the compression stage. Entering the elastic deformation stage, the temperature curve fluctuates horizontally in a low-stress state. When the stress reaches 72.4% of the peak stress, the temperature curve undergoes a short and abrupt decline followed by a smooth decline. Near the specimen failure, the temperature begins to rise rapidly. When the loading is parallel to the bedding, the temperature curve slopes donward almost linearly, mainly during the elastic deformation stage of the specimen. When stress fluctuation occurs in the specimen, the rate of temperature decline decreases. The corresponding temperature curve also slopes up steeply before the specimen failure.

2. The coefficient of variation reflects the degree of dispersion of the surface temperature of oil shale specimens. Due to the existence of the compression stage during the loading perpendicular to the bedding, the closure of bedding cracks will lead to a steep rise of the coefficient of variation curve. The fluctuation of the coefficient of variation curve is very small during the elastic deformation stage irrespective of whether the loading is perpendicular or parallel to the bedding. As the internal stress of the specimen approaches its peak, the horizontally fluctuating curve of the coefficient of variation gradually turns to an abrupt rise, which is mainly caused by the increase of the local temperature due to the cracks expansion and frictional heat generation in the specimen. The point of the turning of the curve from the horizontal fluctuation to an abrupt rise may predict the specimen failure.

3. In the infrared thermal image of the surface of an oil shale specimen, the position of the infrared anomaly precursor is related to the location of internal pores and fractures in and the stress state of the specimen. In the low-stress state of the specimen, a low-temperature anomaly will first appear at locations of cracks inside the specimen; as the stress increases, a high-temperature infrared anomaly will appear at the position of the tips of cracks inside it.

4. During the uniaxial compression of the oil shale specimen, the high-strain region in the strain nephrogram of the specimen surface corresponds to the position of infrared anomaly. The form of infrared anomaly on the specimen surface is related to the characteristics of deformation and mode of failure. Shear failure will occur in a high vertical strain area, and a precursory local high-temperature anomaly will appear in the corresponding position in an infrared thermal image. Tensile failure will occur in a high horizontal strain area, and a precursory local low-temperature anomaly will occur in the corresponding position in the infrared thermal image.

Acknowledgments

REFERENCES

1. Scales, J. A., Batzle, M. Millimeter wave analysis of the dielectric properties of oil shales. *Appl. Phys. Lett.*, 2006, **89**(2), 024102.
2. Du, J., Hu, L., Meegoda, J. N., Zhang, G. Shale softening: Observations, phenomenological behavior, and mechanisms. *Appl. Clay Sci.*, 2018, **161**, 290–300.
3. Zhu, P., Balhoff, M. T., Mohanty, K. K. Compositional modeling of fracture-to-fracture miscible gas injection in an oil-rich shale. *J. Petrol. Sci. Eng.,* 2017, **152**, 628–638.
4. Brandt, A. R., Millard-Ball, A., Ganser, M., Gorelick, S. M. Peak oil demand: the role of fuel efficiency and alternative fuels in a global oil production decline. *Environ. Sci. Technol.,* 2013, **47**(14), 8031–8041.
5. Jiang, X. M., Han, X. X, Cui, Z. G. New technology for the comprehensive utilization of Chinese oil shale resources. *Energy,* 2007, **32**(5), 772–777.
6. Kang, Z. Q., Zhao, Y. S., Yang, D. Physical principle and numerical analysis of oil shale development using in-situ conversion process technology. *Acta Petrol. Sin.,* 2008, **29**(4), 592–595.

7. Masoudian, M. S., Hashemi, M. A., Tasalloti, A., Marshall, A. M. Elastic-brittle-plastic behaviour of shale reservoirs and its implications on fracture permeability variation: an analytical approach. *Rock Mech. Rock Eng.,* 2018, **51**(5), 1565–1582.

8. Vik, H. S., Salimzadeh, S., Nick, H. M. Heat recovery from multiple-fracture enhanced geothermal systems: the effect of thermoelastic fracture interactions. *Renew. Energ.,* 2018, **121**, 606–622.

9. Luo, Y., Xie, H. P., Ren, L., Zhang, R., Li, C. B., Gao, C. Linear elastic fracture mechanics characterization of an anisotropic shale. *Sci. Rep.*, 2018, **8**(1), 8505.

10. Miao, X., Guan, L., Bao, R., Li, Y., Zhan, H., Zhao, K., Xu, F. Layer caused an anisotropic terahertz response of a 3D-printed simulative shale core. *Anal. Sci.,* 2017, **33**(12), 1327–1331.

11. Rahmati, E., Nouri, A., Fattahpour, V., Trivedi, J. J. Numerical assessment of the maximum operating pressure for SAGD projects by considering the intrinsic shale anisotropy. *J. Petrol. Sci. Eng.,* 2017, **148**, 10–20.

12. Wang, M., Li, P., Wu, X., Chen, H. A study on the brittleness and progressive failure process of anisotropic shale. *Environ. Earth Sci.,* 2016, **75**(10), 886.

13. Minaeian, V., Dewhurst, D. N., Rasouli, V. Deformational behaviour of a clay-rich shale with variable water saturation under true triaxial stress conditions. *Geomech. Energy Environ.,* 2017, **11**, 1–13.

14. Cheshomi, A., Hajipour, G., Hassanpour, J., Dashtaki, B. B., Firouzei, Y., Sheshde, E. A. Estimation of uniaxial compressive strength of shale using indentation testing. *J. Petrol. Sci. Eng.,* 2017, **151**, 24–30.

15. Minardi, A., Ferrari, A., Ewy, R., Laloui, L. Nonlinear elastic response of partially saturated gas shales in uniaxial compression. *Rock Mech. Rock Eng.,* 2018, **51**, 1967–1978.

16. Zhou, M., Zhang, Y., Zhou, R., Hao, J., Yang, J. Mechanical property measurements and fracture propagation analysis of Longmaxi shale by micro-CT uniaxial compression. *Energies,* 2018, **11**(6), 1409.

17. Yan, C., Deng, J., Hu, L., Chen, Z., Yan, X., Lin, H., Tan, Q., Yu, B. Brittle failure of shale under uniaxial compression. *Arab. J. Geosci.,* 2015, **8**(5), 2467–2475.

18. Shi, X., Liu, D. A., Yao, W., Shi, Y., Tang, T., Wang, B., Han, W. Investigation of the anisotropy of black shale in dynamic tensile strength. *Arab. J. Geosci.,* 2018, **11**(2), 42.

19. Wu, L., Liu, S., Wu, Y., Wang, C. Precursors for rock fracturing and failure – Part I: IRR image abnormalities. *Int. J. Rock Mech. Min. Sci.,* 2006, **43**(3), 473–482.

20. Qi, K., Tan, Z. Experimental study on acoustoelastic character of rock under uniaxial compression. *Geotech. Geol. Eng.,* 2018, **36**(1), 247–256.

21. Ma, L., Sun, H., Zhang, Y., Zhou, T., Li, K., Guo, J. Characteristics of infrared radiation of coal specimens under uniaxial loading. *Rock Mech. Rock Eng.,* 2016, **49**(4), 1567–1572.

22. Wang, C., Lu, Z., Liu, L., Chuai, X., Lu, H. Predicting points of the infrared precursor for limestone failure under uniaxial compression. *Int. J. Rock Mech. Min. Sci.,* 2016, **88**(10), 34–43.

23. Zhao, Y., Jiang, Y. Acoustic emission and thermal infrared precursors associated

with bump-prone coal failure. *Int. J. Coal Geol.,* 2010, **83**(1), 11–20.

24. Wu, L., Liu, S., Wu, Y., Wu, H. Changes in infrared radiation with rock deformation. *Int. J. Rock Mech. Min. Sci.,* 2002, **39**(6), 825–831.

25. Wu, L., Liu, S., Wu, Y., Wang, C. Precursors for rock fracturing and failure – Part II: IRR T-curve abnormalities. *Int. J. Rock Mech. Min. Sci.,* 2006, **43**(3), 483–493.

26. Wang, X. J. A research on the inorganic carbon dioxide from rock by thermal simulation experiments. *Advances in Earth Science,* 2003, **18**(4), 515–520 (in Chinese).

27. Li, Y.-X., Liu, J.-F. Study on deformation characteristic of surrounding rock by R/S method and fractal theory. *Journal of Sichuan University (Engineering Science Edition)*, 2010, **42**(3), 43–48 (in Chinese).

28. Sun, X., Xu, H., He, M., Zhang, F. Experimental investigation of the occurrence of rockburst in a rock specimen through infrared thermography and acoustic emission. *Int. J. Rock Mech. Min. Sci.,* 2017, **93**, 250–259.

29. Liu, S., Wu, L., Wu, Y. Infrared radiation of rock at failure. *Int. J. Rock Mech. Min. Sci.,* 2006, **43**(6), 972–979.

30. Kivi, I. R., Ameri, M., Molladavoodi, H. An experimental investigation on deformation and failure behavior of carbonaceous Garau shale in Lurestan Basin, west Iran: Application in shale gas development. *J. Nat. Gas Sci. Eng.,* 2018, **55**, 135–153.

31. Liu, L. Q., Chen, G. Q., Liu, P. X., Chen, S. Y., Ma, J. Infrared measurement system for rock deformation experiment. *Seismology & Geology,* 2004, **26**(3), 492–501 (in Chinese).

32. Eberhardt, E., Stead, D., Stimpson, B., Read, R. S. Identifying crack initiation and propagation thresholds in brittle rock. *Can. Geotech. J.,* 1998, **35**(2), 222–233.